

# Hybrid Microsupercapacitors with Vertically Scaled 3D Current Collectors Fabricated using a Simple Cut-and-Transfer Strategy

Qiu Jiang, Narendra Kurra, Chuan Xia, and Husam N. Alshareef\*

On-chip energy storage devices, including thin film batteries and microsupercapacitors, are being developed as micropower ( $\mu$ -power) units for portable electronic devices, self-powered systems, and internet-of-things applications.<sup>[1]</sup> However, thin film and 3D microbatteries often suffer from poor rate performance and cycle life. In comparison, microsupercapacitors have shown promise as micropower sources with high power density, fast charge–discharge rates, and long cycle life, but often with limited energy density. The trade-off between the energy and power densities can be improved by proper selection of electrode materials, current collector design, and device configuration. In that respect, coplanar hybrid microsupercapacitors with vertically scaled, 3D porous current collectors may be a key strategy in enhancing areal energy and power densities.

Conventional microfabrication techniques have been widely employed in fabricating various state-of-the-art carbon based microsupercapacitors.<sup>[2,3]</sup> Further, pseudocapacitive materials such as metal oxides/hydroxides,<sup>[4]</sup> sulfides,<sup>[5]</sup> and conducting polymers<sup>[6]</sup> were used in enhancing the capacity and energy density of on-chip electrochemical devices. In practice, key electrochemical performance metrics of on-chip energy storage rely on the energy and power density in a given footprint area.<sup>[1]</sup> However, microsupercapacitors fabricated by conventional photolithography often suffer from limited mass loadings of active materials in a given footprint area ( $<0.1 \text{ mg cm}^{-2}$ ). One of the approaches is to deposit thicker electrode films to achieve higher areal energy density, but thicker electrodes may suffer from poor mechanical stability, poor adhesion, and high resistivity, which could impede the electron/ion transport, resulting in mediocre power performance of the device.

The technological trend to achieve high areal performance is to transition from 2D to 3D architecture, where an optimal mass loading of active material can be achieved in a given footprint area. For instance, silicon-based microelectromechanical systems (MEMS) technology was employed in fabricating various 3D microsupercapacitors. Further, 3D arrays of Si (30  $\mu\text{m}$  thick) and SU-8 (100  $\mu\text{m}$  thick) were fabricated as scaffolds for increasing loading of active materials compared to 2D collector counterparts.<sup>[7]</sup> However, thicker coatings (50–150  $\mu\text{m}$ ) of

$\text{MnO}_2$  and activated carbons employing binders and conductive additives, which are electrochemically inactive, often have poor electrochemical performance due to limited diffusion kinetics of electrolyte ions. In the case of thick block of electrode materials, electrolyte permeability is hindered and charge extraction becomes inefficient, which limits the final electrochemical performance of such devices. Therefore, compared to planar current collectors, ultrathick current collectors such as Ni foam or carbon fiber cloth are the best choice in terms of direct growth of electroactive materials by various methods on 3D collectors. This is because their intrinsic macroporous nature helps maximize active material loading, while providing easy access to the electrolyte ions, leading to faster reaction kinetics and hence improved electrochemical performance. For example, Ni foam has been extensively used in direct growth of metal oxides and sulfides by hydrothermal method<sup>[8,9]</sup> resulting in excellent specific capacity values. However, there are no reports on fabrication of coplanar electrochemical devices (e.g., microsupercapacitors) based on Ni foam patterned collectors. Since Ni foam is bulky (thickness of 500–1200  $\mu\text{m}$ ) with porous texture, it is not amenable to patterning by conventional photolithography.

Here, we propose a new strategy for patterning macroscopic ultrathick 3D current collectors in the form of interdigitated electrodes by laser machining. A robust and simple approach was developed to pattern 3D current collectors as frameworks for maximum electroactive material loading with optimal electrochemical performance in a given footprint area. This platform can be used to evaluate various active materials in coplanar hybrid (asymmetric) configuration, which is typically more difficult to fabricate in comparison to symmetric configuration. As a proof of concept, a hybrid device is demonstrated, employing Faradaic  $\text{NiCo}_2\text{S}_4$  as a positive electrode material and electrochemical double-layer carbon nanofiber (CNF) as a negative electrode, both of which were directly grown on Ni foam interdigital electrodes by hydrothermal and chemical vapor deposition methods, respectively. We have demonstrated the fabrication of the hybrid coplanar device with remarkable areal capacity in a given footprint area with high operating voltage window in aqueous and gel electrolytes. Indeed, this hybrid prototype device exhibits superior energy density of  $200 \mu\text{Wh cm}^{-2}$  compared to state-of-the-art microsupercapacitors ( $1\text{--}40 \mu\text{Wh cm}^{-2}$ ), with higher power density when compared to thin-film batteries and microbatteries at comparable energy density.

Laser engraving is a direct patterning method, involving neither photoresists nor complicated multistep processing. Thanks to the energetic laser beam which has the ability to cut the metals locally, desired object shapes for many applications can

Q. Jiang, Dr. N. Kurra, C. Xia, Prof. H. N. Alshareef  
Materials Science and Engineering  
King Abdullah University of Science and  
Technology (KAUST)  
Thuwal 23955-6900, Saudi Arabia  
E-mail: husam.alshareef@kaust.edu.sa



DOI: 10.1002/aenm.201601257

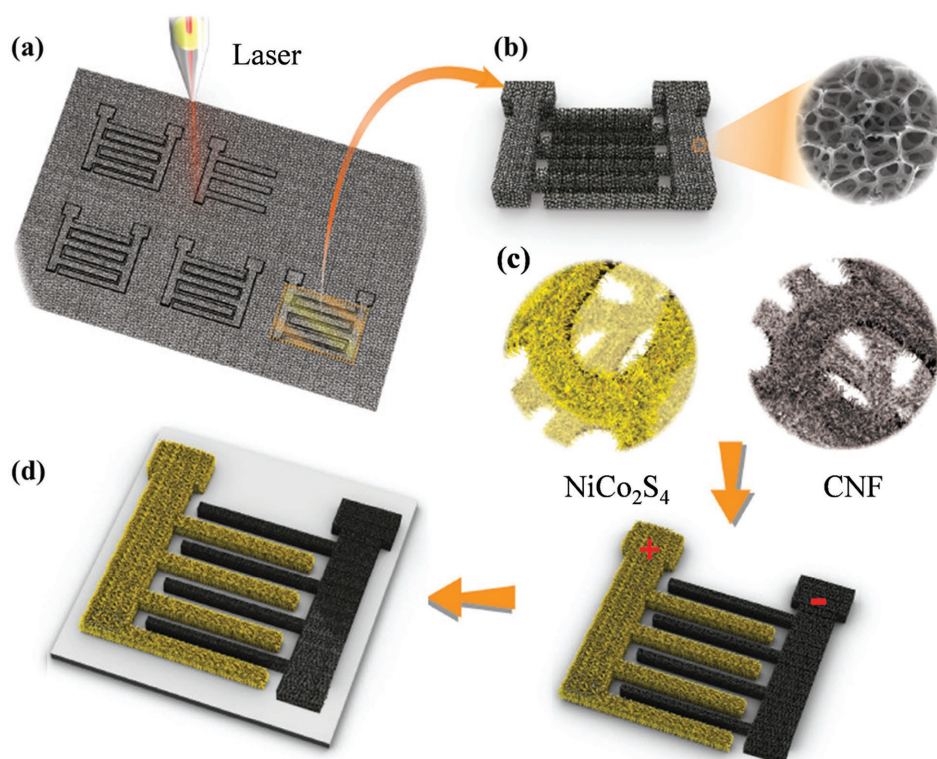


**Figure 1.** Schematic illustrating fabrication of the hybrid devices. a) Laser machining of ultrathick nickel foam in the form of interdigitated designs. b) Ni foam 3D interdigital current collectors. c)  $\text{NiCo}_2\text{S}_4$  and CNF are separately grown on individual interdigitated 3D Ni-foam collectors. d) Hybrid device with positive  $\text{NiCo}_2\text{S}_4$  and negative CNF is transferred to a glass substrate using a thin PDMS layer.

be carved out. For instance, simple laser-cut interdigitated electrodes could constitute coplanar architecture of a capacitive element. As shown in **Figure 1a**, laser machining was employed to create interdigitated electrode patterns out of ultrathick nickel foam (NF). The laser-based technique is found to be a versatile approach since it can be employed to pattern bulk current collectors such as carbon cloth and Ni foam in a single step and direct manner (see Figure S1 in the Supporting Information). Detailed geometric parameters of the collector design are listed in Table S1 in the Supporting Information. The honeycomb-type structure with associated macroporosity of the Ni foam is beneficial to achieve maximum loading of the active materials in a binder-free manner. The crosslinked honeycomb-type morphology of Ni foam is illustrated in the inset of Figure 1b. Ni foam has been extensively used to grow various classes of materials ranging from carbon nanotubes,<sup>[10]</sup> graphene<sup>[11]</sup> grown by chemical vapor deposition and metal oxides,<sup>[9,12]</sup> sulfides,<sup>[13,14]</sup> selenides,<sup>[15]</sup> grown by hydrothermal synthesis. Most of these studies have focused on three-electrode measurements to estimate the specific capacitance of the deposited electrode materials. However, for practical applications, two-electrode stack or coplanar configuration is more relevant. Here, a novel strategy of using direct-laser cutting is proposed to fabricate co-planar electrode architectures of Ni foam electrodes. Laser engraving was employed to cut through the Ni foam of various thicknesses (500, 700, or 1200  $\mu\text{m}$ ). No photoresist is used in this single-step process. This technique is fast, cost-effective, scalable, and has been successfully used in our laboratory to

produce interdigitated 3D current collectors. The intrinsic macroporosity and high electronic conductivity of the Ni foam makes it an ideal 3D framework for optimal mass loading of electroactive materials. The robustness of the Ni metal current collectors allows depositing various carbon based or pseudocapacitive materials at various temperatures, pressure, and chemical conditions. For instance, as Ni foam can sustain a wide range of temperatures (from room temperature up to 1000  $^{\circ}\text{C}$ ), and chemical environments for growth of a plethora of materials, it could make an ideal platform for fabricating coplanar 3D microsupercapacitors. After laser machining, the obtained NF collector fingers were placed in a teflon-lined autoclave for hydrothermal synthesis to grow nickel cobalt sulfide ( $\text{NiCo}_2\text{S}_4$ ) directly, while carbon nanofiber was grown directly on the other NF collector fingers by chemical vapor deposition (CVD) (see Figure 1c). These separate interdigital electrodes were transferred onto a glass substrate by a bottom polydimethylsiloxane (PDMS) layer while applying mild pressure for firm contact, resulting in hybrid coplanar supercapacitor device as shown in Figure 1d. Therefore, this technique can be used for patterning macroscopic ultrathick current collectors into coplanar energy storage devices.

Ternary nickel cobalt sulfide nanotubes were directly grown on Ni foam in a two-step hydrothermal method to avoid the use of binder and conductive additives which have no contribution to the overall capacitance,<sup>[16]</sup> while ensuring better electrical contact between active material and the current collector for facile electron transport. The crystalline nature of  $\text{NiCo}_2\text{S}_4$

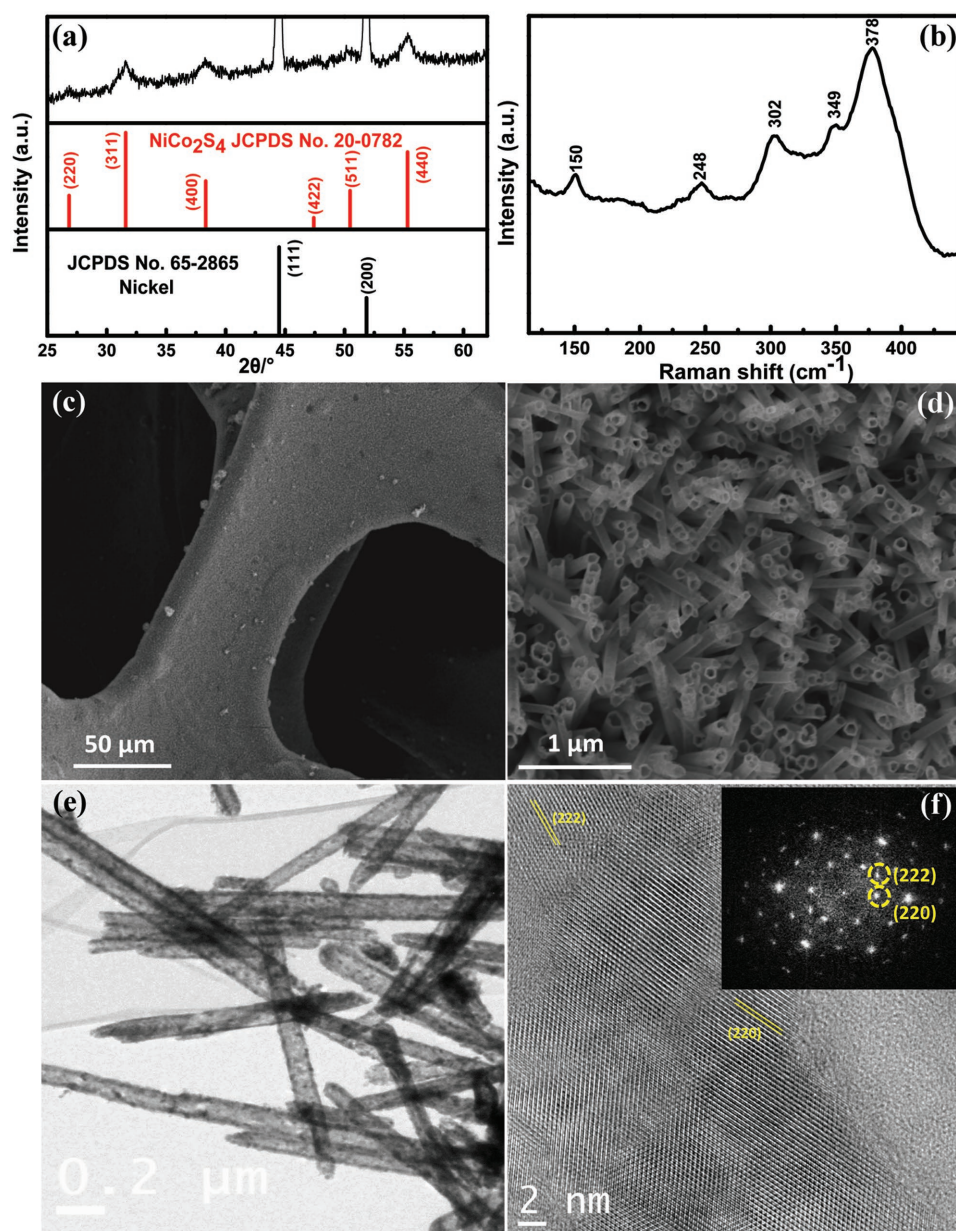


**Figure 2.** a) Typical XRD pattern and b) Raman spectrum of the  $\text{NiCo}_2\text{S}_4$  nanotubes directly grown on Ni foam. c) Low and d) high magnification SEM images of the  $\text{NiCo}_2\text{S}_4$  nanotubes. e–f) TEM images of the  $\text{NiCo}_2\text{S}_4$  nanotubes, inset of (f) shows the corresponding SAED pattern.

was investigated by X-ray diffraction (XRD) and the diffraction pattern is shown in **Figure 2a**. The two strongest peaks at  $44.5^\circ$  and  $51.8^\circ$  are assigned to the diffraction from the (111) and (220) planes of Ni foam substrate. All remaining peaks at  $2\theta$  values of  $31.6^\circ$ ,  $55.3^\circ$ ,  $38.3^\circ$ ,  $50.5^\circ$ ,  $26.8^\circ$ , and  $47.4^\circ$  are very well matched to the nanostructured cubic type  $\text{NiCo}_2\text{S}_4$  (JCPDS 20-0782), without any secondary phases. The relative intensities of  $\text{NiCo}_2\text{S}_4$  peaks are seen quite low because the underlying Ni foam diffracts significantly. Raman spectrum was recorded under Ar atmosphere to avoid laser induced oxidation of sulfides in the presence of air.<sup>[17]</sup> As shown in **Figure 2b**, the peak at  $378\text{ cm}^{-1}$  can be ascribed to the stretching of sulfur atom toward the tetrahedral site Ni atom, while the character-

istic peak at  $248\text{ cm}^{-1}$  can be assigned to the bending vibration of S–Ni–S bonds, matching with previous reports.<sup>[17]</sup> The remaining three peaks at 150, 302, and  $349\text{ cm}^{-1}$  can be attributed to the asymmetric bending of the S–Ni–S bonds. Energy-dispersive X-ray (EDX) and X-ray photoelectron spectroscopy (XPS) analysis presented in Figures S2 and S3 in the Supporting Information are consistent with the above results. **Figure 2c** shows the typical low-magnification field emission scanning electron microscopy (FESEM) image of as-grown  $\text{NiCo}_2\text{S}_4$  on Ni foam. The  $\text{NiCo}_2\text{S}_4$  layer appears to be fairly uniform while retaining the macroscopic conformal coating over the entire Ni foam. At higher magnification, hollow nanotube morphology of  $\text{NiCo}_2\text{S}_4$  is observed, as shown in **Figure 2d**. Typical length



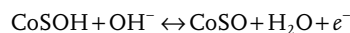
and diameter of the nanotubes are estimated to be  $1 \pm 0.5 \mu\text{m}$  and  $100 \pm 50 \text{ nm}$ , respectively. The growth process and structure of our nanostructured  $\text{NiCo}_2\text{S}_4$  on Ni foam is similar to the process reported by Ma et al. recently.<sup>[18]</sup> The formation of hollow tube morphology can be explained by Kirkendall effect that has been widely employed to create interior voids in metal sulfides. This can be explained as follows. Released  $\text{S}^{2-}$  ions react with metal ions to form a thin layer of  $\text{NiCo}_2\text{S}_4$  on the surface of metal carbonate hydroxide nanowires, and that thin layer acts as a physical barrier to prevent the direct reaction between the external  $\text{S}^{2-}$  with inner metal carbonate hydroxide. Accordingly, further reaction is controlled largely by the diffusion of metal ions or  $\text{S}^{2-}$  through this thin  $\text{NiCo}_2\text{S}_4$  layer. Since the rate of outward diffusion of the small metal ions is much greater than the rate of inward diffusion of the bulky  $\text{S}^{2-}$  ions, further sulfurization is mostly confined to the outer surface of the  $\text{NiCo}_2\text{S}_4$  layer, creating hollow structure.<sup>[13,19]</sup> These hollow structures can increase the electrode surface area while facilitating the electrolyte penetration. The TEM image shown in Figure 2e further confirms the morphology of the  $\text{NiCo}_2\text{S}_4$  tube structure. The lattice plane spacings are calculated to be 2.6 and 3.2 nm from high-resolution transmission electron microscopy (HRTEM) in Figure 2f, which correspond to the (220) and (222) planes of Linnaeite phase.<sup>[20]</sup> Different orientations of the fringes reveal the polycrystalline nature of the material,<sup>[17]</sup> which is further confirmed by the selected area electron diffraction (SAED) pattern shown in the inset of Figure 2f.

Electrochemical properties of individual  $\text{NiCo}_2\text{S}_4/\text{NF}$  and  $\text{CNF}/\text{NF}$  components were studied in the positive and negative potential windows in a three-electrode configuration using 1 M potassium hydroxide (KOH) aqueous electrolyte. We have investigated the role of thickness of Ni foam and mass loading of  $\text{NiCo}_2\text{S}_4$  in optimizing its specific capacity. Initially, Ni foams with three different thicknesses of 500, 700, and 1200  $\mu\text{m}$  (denoted as NF-500, NF-700, and NF-1200, with the same areal mass density of nickel) were chosen in order to study the vertical (thickness) scaling effect. To have a fair comparison, mass loadings of  $\text{NiCo}_2\text{S}_4$  were maintained constant at  $2.5 \text{ mg cm}^{-2}$  for these three NF thicknesses (the mass loading can be controlled by the concentration of the reacted precursor solution). As shown in Figure 3a, areal capacities were calculated from galvanostatic discharge curves (see Figure S5 in the Supporting Information) and are plotted for different values of Ni foam thicknesses. Areal capacity as much as  $550 \mu\text{A h cm}^{-2}$  (corresponding gravimetric capacity of  $220 \text{ mA h g}^{-1}$ ) is achieved at a current density of  $7 \text{ mA cm}^{-2}$  for  $\text{NiCo}_2\text{S}_4/\text{NF}$ -1200 at a mass loading of  $2.5 \text{ mg cm}^{-2}$ . The estimated areal capacitance of  $4000 \text{ mF cm}^{-2}$  (potential window, 0.8 V) is found to be better than the best reported value of  $3700 \text{ mF cm}^{-2}$  for  $\text{RuO}_2/3\text{D}$  gold current collector.<sup>[21]</sup> As expected, when the thickness of Ni foam decreases, the areal capacity is reduced even for similar mass loading of  $\text{NiCo}_2\text{S}_4$ . This could be due to the fact that at a given mass loading, the effective growth thickness of  $\text{NiCo}_2\text{S}_4$  might be lower on NF-1200 as compared to NF-500. Further, for a given thickness of NF (for example, NF-1200), the mass loading was controlled to obtain maximum specific capacity. At this stage, it is also important to estimate the contribution from the bare NF itself which should be subtracted from the total capacity shown by  $\text{NiCo}_2\text{S}_4/\text{NF}$ . It was found that NF

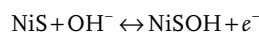
contribution is only 5% (total specific capacity of  $\text{NiCo}_2\text{S}_4/\text{NF}$  is  $550 \mu\text{A h cm}^{-2}$  while NF shows capacity of  $30 \mu\text{A h cm}^{-2}$ , see Figure S6 in the Supporting Information), which is negligible when compared to overall capacity.

NF-1200 was chosen to estimate the areal capacity with respect to mass loading. As shown in Figure 3b, areal capacities for different mass loadings of 1.8, 2.5, 3.2, and  $5.4 \text{ mg cm}^{-2}$  were compared. At a current density of  $7 \text{ mA cm}^{-2}$ , as the mass loading is increased from 1.8 to  $2.5 \text{ mg cm}^{-2}$ , areal capacity is also increasing from 330 to  $550 \mu\text{A h cm}^{-2}$ . When mass loading is further increased, a reduction in areal capacity was observed, which could be explained by the increased ionic/electronic resistance of thicker films. Thus, maximum areal capacity is achieved when mass loading of the active material is  $\approx 2.5 \text{ mg cm}^{-2}$ . The increased/decreased specific capacity with mass loadings can originate from changes in the nanostructure and conductivity of the active material (see Figure S7 in the Supporting Information). The larger surface area increases the number of electroactive sites where electrochemical reactions can take place, and increases wettability and permeability of the electrolyte. Similar effect of mass loading has also been reported for porous  $\text{MnO}_2$  electrode.<sup>[22]</sup> The corresponding converted gravimetric capacity also showed a similar trend with increasing mass loading (Figure S7 and S8, Supporting Information).

Typical CVs of the  $\text{NiCo}_2\text{S}_4/\text{NF}$ -1200 (mass loading of  $2.5 \text{ mg cm}^{-2}$ ) are shown in Figure 3c, where two pairs of redox peaks are observed. These peaks can be attributed to the reversible Faradaic reactions of  $\text{Co}^{2+}/\text{Co}^{3+}/\text{Co}^{4+}$  and  $\text{Ni}^{2+}/\text{Ni}^{3+}$  in aqueous alkaline solution. The first pair of redox peaks at lower potentials (0.33 V) can be explained by the following reactions



while the second pair of peaks at 0.38 V can be attributed to the redox reaction of  $\text{Ni}^{2+}/\text{Ni}^{3+}$ .



At higher scan rates, shifts in the redox potentials toward more positive/negative potentials were observed, which is caused by diffusion limitations associated with the redox processes.

To gain more insight into the charge storage mechanism of  $\text{NiCo}_2\text{S}_4$ , sweep analysis was done to quantify the capacity contribution from capacitive and diffusion-controlled processes. The total current as a function of potential can be expressed as a sum of diffusion controlled Faradaic processes and double layer capacitive currents, as shown by the following equation

$$i(V) = k_1 v + k_2 v^{1/2} \quad (1)$$

where  $v$  is the scan rate ( $\text{mV s}^{-1}$ ),  $k_1 v$  and  $k_2 v^{1/2}$  represent the currents from surface capacitance contribution and the diffusion-controlled Faradaic process, respectively.<sup>[23]</sup> Equation (1) can also be rearranged to

$$i(V)/v^{1/2} = k_1 v^{1/2} + k_2 \quad (2)$$

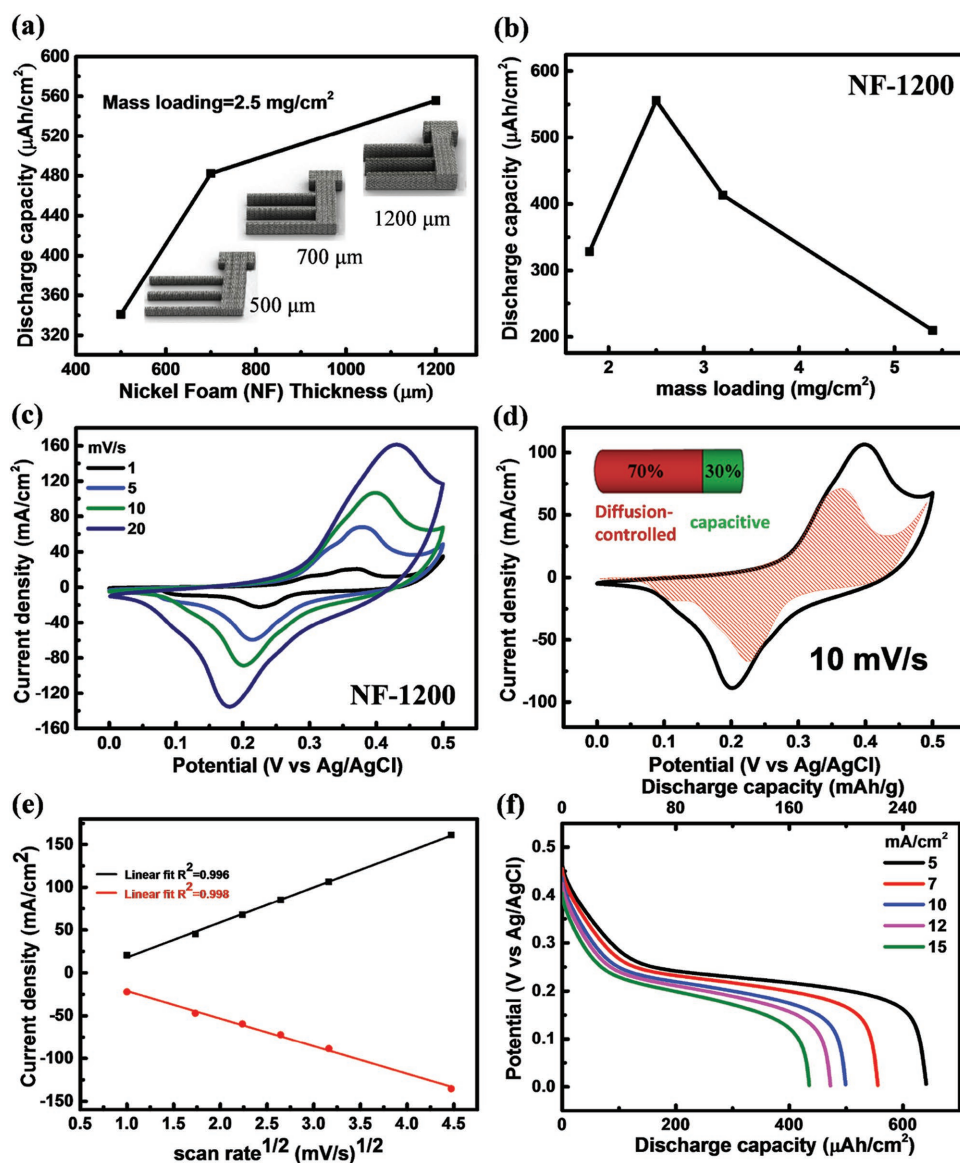


**Figure 3.** a) Areal specific capacity versus thicknesses of 3D Ni foam measured at 7 mA cm<sup>-2</sup> in 1 M KOH aqueous electrolyte. b) Areal specific capacity versus mass loading for the NF-1200. c) Typical CV curves of NiCo<sub>2</sub>S<sub>4</sub>/NF (mass loading 2.5 mg cm<sup>-2</sup>, 3D Ni Foam thickness is 1200 μm). d) Diffusion controlled charge storage contribution is shown as shaded area of CV curve at 10 mV s<sup>-1</sup> (solid line). e) Anodic and corresponding cathodic peak current densities (presented in (c)) versus the square root of scan rate. f) Galvanostatic discharge curves at various current densities.

So  $K_1$  and  $k_2$  can be derived from the linear plot from  $i(V)/v^{1/2}$  versus  $v^{1/2}$  with different scan rates from Figure 3c. Relative capacitive and Faradaic contributions are estimated to be 70% and 30%, respectively (see Figure 3d). It was also observed that the peak current varies linearly with the square root of the scan rate (Figure 3e), which again confirms the diffusion limited nature of the redox reaction.<sup>[24]</sup>

Galvanostatic discharge curves of NiCo<sub>2</sub>S<sub>4</sub>/NF at different current densities are shown in Figure 3f. Clear potential plateaus present at around 0.25 V confirm the Faradaic process, matching well with the potentials corresponding to the redox peaks observed in the CV curves. The NiCo<sub>2</sub>S<sub>4</sub>/NF electrodes deliver a specific capacity of 640 μA h cm<sup>-2</sup> (specific gravimetric capacity of 256 mA h g<sup>-1</sup>) at 5 mA cm<sup>-2</sup> (2 A g<sup>-1</sup>) and

retain specific capacity of 435 μA h cm<sup>-2</sup> (174 mA h g<sup>-1</sup>) at 15 mA cm<sup>-2</sup> (6 A g<sup>-1</sup>) with capacity retention of 70%. The good rate capabilities can be attributed to the electrically conductive nature of NiCo<sub>2</sub>S<sub>4</sub> itself<sup>[17]</sup> and the rational design of nanostructured materials grown directly on the current collector. It is possible that the 3D nanostructured hollow nanotube morphology shortens the ion diffusion path for mass transport and at the same time gives access to more active sites since no binder was used. It is also likely that the direct contact between the NiCo<sub>2</sub>S<sub>4</sub> nanotubes and NF reduces the interfacial impedance and thus contributes to fast electron transportation with shortened ion diffusion pathways.

Carbon nanofibers were grown directly on Ni foam by CVD, and they were then employed as the negative electrode

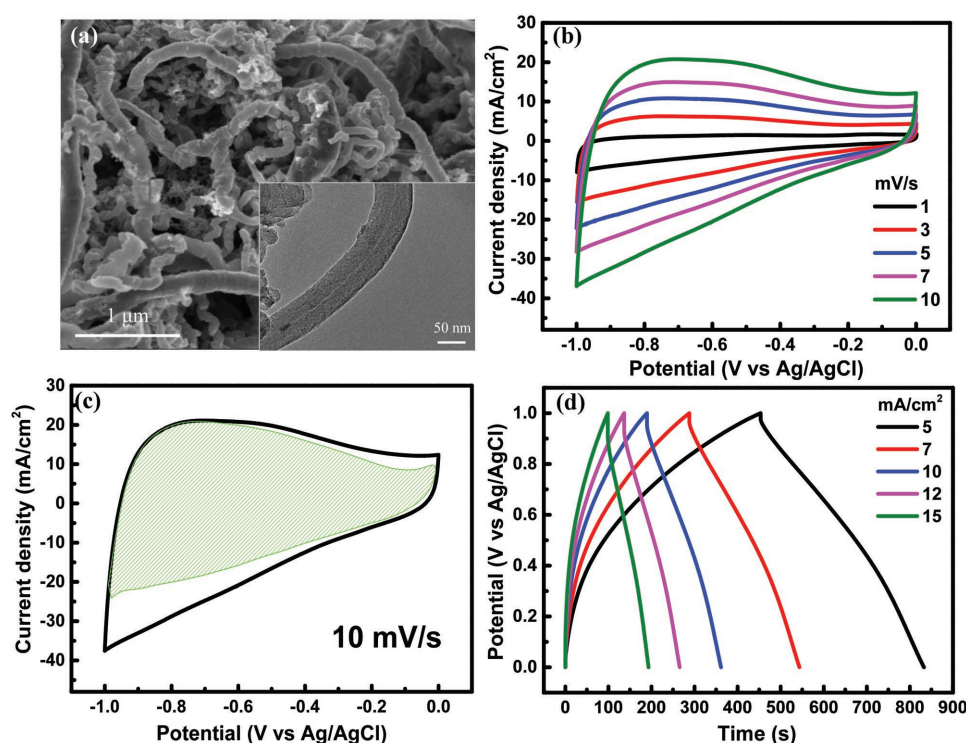


**Figure 4.** a) SEM and TEM (inset) images of the carbon nanofibers (CNFs) grown on interdigitated Nickel foam collector. b) Cyclic voltammograms; c) deconvolution of charge storage contributions of CNF from capacitive component at a scan rate of 10 mV s<sup>-1</sup>. d) Galvanostatic charge-discharge profiles of CNF/NF in 1 M KOH.

because of their 1D conductivity, efficient ion diffusion pathways<sup>[25]</sup> and easy control of mass loading. The SEM image in **Figure 4a** shows the compact coating of the randomly oriented CNF on Ni foam. A low-magnification TEM image of the carbon nanofibers is shown in the inset of **Figure 4a**, where rope-like morphology with very thin hollow core and catalyst particle inside, is observed. The structural aspects of CNF were further investigated by Raman spectroscopy (**Figure S10**, Supporting Information). The two strongest peaks appear around 1350 (FWHM 115 cm<sup>-1</sup>) and 1580 cm<sup>-1</sup> (Full width at half maximum (FWHM) 80 cm<sup>-1</sup>) are assigned to the D and G bands of CNF, respectively. A small peak at 2700 cm<sup>-1</sup> corresponds to 2D band which is a signature for the *c*-axis periodicity of graphene layers of CNF. The ratio of the intensity of D and G bands,  $I_D/I_G$  is found to be 1.1. The mean  $sp^2$  crystallite size ( $L_a$ ) is estimated to be  $\approx 11$  nm by using the formula<sup>[26]</sup>

$$L_a \text{ (nm)} = (2.4 \times 10^{-10}) \lambda^4 \left( \frac{I_D}{I_G} \right)^{-1} \quad (3)$$

where  $\lambda$  is the laser excitation wavelength in nm.

As shown in **Figure 4b**, CVs of CNF grown on Ni foam show no obvious Faradaic current, indicating electrochemical double layer behavior. No obvious hydrogen evolution is observed until a potential of -1 V, indicating that the CNF/NF behaves as a negative electrode. From Equation (2), we conclude that the main contribution of the capacitance (80%) is attributed to the fast surface reactions (**Figure 4c**). The galvanostatic charge/discharge curves in **Figure 4d** show typical symmetric

triangular-shape curves, which are due to the electrochemical double layer adsorption of electrolyte ions. The Ohmic drop is small even at a high current density of 40 mA cm<sup>-2</sup>, implying good electrical conductivity of CNF electrodes.<sup>[27]</sup>

Charge on the positive and negative electrodes was balanced by adjusting the mass loading of CNFs on the negative electrode and the corresponding charge balance chart is shown in **Table S2** in the Supporting Information. Hybrid devices were assembled by gluing the two well-defined comb electrodes onto the glass substrate having a thin layer of PDMS under an optical microscope. As shown in **Figure 5a**, CVs of the hybrid devices show no obvious oxygen evolution (no sudden rise in the current at higher potentials). Even when the voltage window is extended up to 1.6 V, the shape of the CVs shows typical redox behavior, indicating the dominating Faradaic behavior of the hybrid supercapacitors. To investigate the charge storage mechanism in the hybrid device, diffusion controlled and capacitive currents are separately extracted from the CV curve at a scan rate of 10 mV s<sup>-1</sup>, as shown in **Figure 5b**. It is estimated that 56% of the total current comes from diffusion controlled processes, while the remaining 44% come from capacitive type processes. This analysis clearly shows that the hybrid device possesses characteristics of both EDLC and Faradaic components, which is further confirmed by the quasi-voltage plateaus shown in the galvanostatic discharge curves (**Figure 5d**). This type of behavior may be referred to as aqueous battery behavior; however, the fast response of the hybrid device even at a higher scan rate of 50 mV s<sup>-1</sup> qualifies it as a capacitive device. **Figure 5c** shows the CVs of positive and negative electrodes in



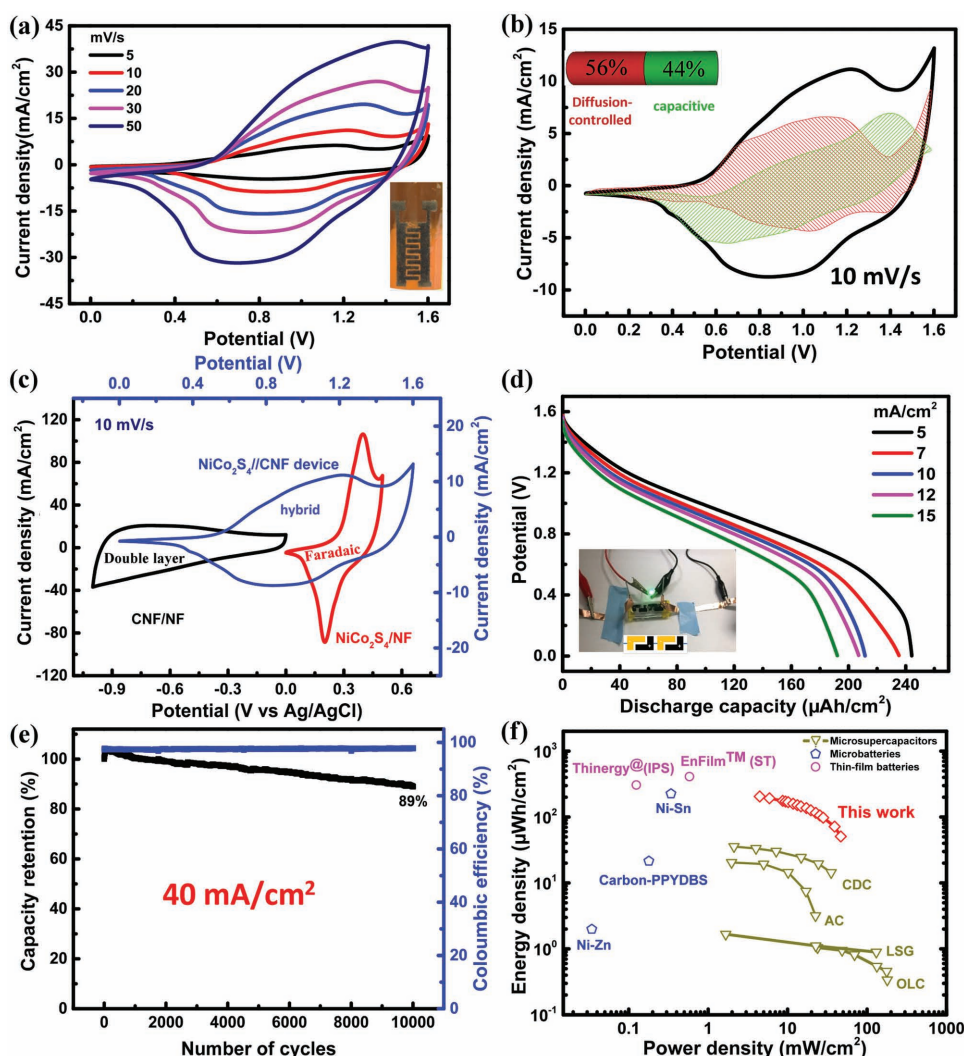


**Figure 5.** Electrochemical performance of  $\text{NiCo}_2\text{S}_4//\text{CNF}$  device. a) Cyclic voltammograms of the  $\text{NiCo}_2\text{S}_4//\text{CNF}$  hybrid device, inset shows the device attached to the polyimide sheet. b) Voltammetric response at  $10 \text{ mV s}^{-1}$ . Solid line represents total current from experiment, diffusion controlled current (red shaded region), and capacitive current (green shaded region) are derived from (a). c) CVs of  $\text{NiCo}_2\text{S}_4/\text{NF}$ ,  $\text{CNF}/\text{NF}$  electrodes, and  $\text{NiCo}_2\text{S}_4//\text{CNF}$  device at a scan rate of  $10 \text{ mV s}^{-1}$ . d) Galvanostatic discharge curves at different current densities of the  $\text{NiCo}_2\text{S}_4//\text{CNF}$  device, inset shows series connected devices were able to glow a LED. e) Cycling stability and Coulombic efficiency of the hybrid device over 10 000 cycles in  $1 \text{ M KOH}$  electrolyte. f) Ragone plot showing the areal energy and power densities of commercial thin-film batteries, state-of-the-art microbatteries, and microsupercapacitors compared to the hybrid microsupercapacitor fabricated in this study.

the complementary potential windows, along with the resultant hybrid device with extended voltage operation (up to  $1.6 \text{ V}$ ). In three-electrode measurement, CV curves of individual  $\text{NiCo}_2\text{S}_4/\text{NF}$  electrode show two pronounced redox peaks within the potential window of  $0\text{--}0.5 \text{ V}$ , which clearly shows the Faradaic nature of the positive electrode as described earlier. While CV curves of the individual  $\text{CNF}/\text{NF}$  electrode mainly exhibit a quasi-rectangular shape in the negative potential window of  $-1$  to  $0 \text{ V}$ , clearly showing electric double layer behavior. Thus, our hybrid device has combined the Faradaic and double layer electrodes to increase the operating voltage of the aqueous electrolyte in order to achieve higher energy and power densities of the hybrid supercapacitor. Broad redox peaks are observed in the CV curves of the hybrid supercapacitor (2-electrode configuration). The inset of Figure 5d shows that two series connected

tandem devices are capable of glowing a green LED (a few seconds charging is enough in glowing LED for a minute). The device delivers a capacity of  $240 \mu\text{A h cm}^{-2}$  at  $5 \text{ mA cm}^{-2}$  and retains  $190 \mu\text{A h cm}^{-2}$  at  $15 \text{ mA cm}^{-2}$ , indicating good rate performance (79%). A capacity of  $240 \mu\text{A h cm}^{-2}$  at  $5 \text{ mA cm}^{-2}$  can be retained even after deep cycling at  $15 \text{ mA cm}^{-2}$ , which shows good cycling performance (see Figure S11 in the Supporting Information). Long-term cycling tests were performed in  $1 \text{ M KOH}$  electrolyte at high current density of  $40 \text{ mA cm}^{-2}$  over 10 000 cycles (Figure 5e), which indicate that 89% of the initial discharge capacity was retained. The improved cycling performance of the device compared with  $\text{NiCo}_2\text{S}_4/\text{NF}$  (67% after 10 000 cycles, see Figure S9 in the Supporting Information) can be attributed to the introduction of EDLC type negative electrode material. Electrochemical performance of our hybrid

device is compared with other state-of-the-art energy storage devices as shown in the Ragone plot in Figure 5f. Our device shows an energy density of  $200 \mu\text{Wh cm}^{-2}$  at a power density of  $4.4 \text{ mW cm}^{-2}$ ; at high power density of  $45 \text{ mW cm}^{-2}$ , excellent energy density of  $49 \mu\text{Wh cm}^{-2}$  can still be maintained. These energy densities are superior to advanced microsupercapacitors,<sup>[3,28]</sup> Ni–Zn<sup>[21]</sup> micro-batteries ( $3 \mu\text{Wh cm}^{-2}$ ), and is comparable to commercial thin-film batteries ( $350 \mu\text{Wh cm}^{-2}$ )<sup>[21]</sup> and Ni–Sn<sup>[21]</sup> microbatteries ( $230 \mu\text{Wh cm}^{-2}$ ), while high power density can be delivered. To demonstrate a practical application, electrochemical performance of the solid-state device (with gel electrolyte) is also tested (see Figure S12 in the supporting information).

It is worth mentioning a few merits of this study. A new paradigm of direct patterning of ultrathick (3D) macroporous current collectors is demonstrated as a promising strategy for enhanced areal performance of coplanar electrochemical devices. Direct growth of electroactive materials at higher mass loadings ( $>1 \text{ mg cm}^{-2}$ ) while providing easy access to electrolyte ions paves the way to achieving better electrochemical performance of the devices. It has to be noted that the resolution of the laser patterning technique should not be compared with the sophisticated microfabrication techniques such as lithography and nanoimprinting. There is a trade-off that often exists between resolution and simplicity. As we are patterning ultrathick (up to  $1200 \mu\text{m}$  thick) macroporous Ni foam substrate, resolution is expected to be lower than lithography methods. Therefore, though we sacrificed electrode spacing at the expense of higher mass loading of active materials with an asymmetric design to widen the operating voltage window of the supercapacitor, ultimately excellent energy and power densities were achieved. Having said this, the large electrode spacing could negatively impact the diffusion of ions during the charge/discharge process.<sup>[29]</sup> However, we envision that by automating the placement of the current collectors on substrates, one could have better control over finger spacing than in our manual, proof-of-concept approach.

In summary, a direct-write strategy has been proposed for fabricating ultrathick (3D) coplanar hybrid supercapacitors. The key aspect of this study lies in the increase of active material mass in a given area by exploiting the third dimension of the energy storage device. The proposed “cut-and-transfer” method, while manually cumbersome, can be automated to scale down the size and to meet the required voltage/power ratings. Using this approach, we have demonstrated hybrid micro-supercapacitors with high areal energy density ( $200 \mu\text{Wh cm}^{-2}$ ) and excellent cycling stability (capacity retention of 89% after 10 000 cycles). The high areal energy density may meet the demand of on-chip storage for the next generation of integrated microsystems.

## Experimental Section

**Experimental Materials:** Chemicals were used as received without further purification. Analytical grade cobalt(II) nitrate ( $\text{Co}(\text{NO}_3)_2 \cdot 6\text{H}_2\text{O}$ ), nickel(II) nitrate ( $\text{Ni}(\text{NO}_3)_2 \cdot 6\text{H}_2\text{O}$ ), and urea ( $\text{NH}_2\text{CONH}_2$ ) were purchased from Sigma-Aldrich. Sodium sulfide nanohydrate ( $\text{Na}_2\text{S} \cdot 9\text{H}_2\text{O}$ ) was purchased from Acros Organics. Elastomer and curing agent of PDMS (base/curing agent, Sylgard 184, Dow Corning) were

purchased from Dow. Porous Ni foams (areal mass density of  $320 \text{ g m}^{-2}$ , thicknesses of 500, 700, and  $1200 \mu\text{m}$ ) were purchased from Shanghai Tools Co., Ltd.

**Fabrication of Interdigitated 3D Ni Patterns:** Briefly, Ni foam (NF) of various thicknesses was first sonicated in 1 M hydrochloric acid for 10 min to dissolve away the surface oxide layer and then thoroughly washed with deionized (DI) water followed by drying off with nitrogen gas.  $\text{CO}_2$  Universal Laser cutter System (model: Professional laser system PLS6.75, wavelength of  $10.6 \mu\text{m}$ ) was used to fabricate interdigitated 3D Ni patterns by direct laser engraving. The averaged focused beam size is around  $120 \mu\text{m}$ . Laser power was set to 75 W at a scan rate of  $0.2 \text{ cm s}^{-1}$  and pulse per inch was always set to 1000 to avoid serrated or perforated-looking edge. After the whole cutting process, total area of the interdigitated device is around  $2.3 \text{ cm}^2$ . All these experiments were carried out at room temperature with compressed air flow.

**Synthesis of  $\text{NiCo}_2\text{S}_4$  on Ni Foam:** All reagents in the experiment are of analytical grade. Briefly,  $12.5 \times 10^{-3} \text{ M}$   $\text{Ni}(\text{NO}_3)_2 \cdot 6\text{H}_2\text{O}$ ,  $25 \times 10^{-3} \text{ M}$   $\text{Co}(\text{NO}_3)_2 \cdot 6\text{H}_2\text{O}$ , and  $50 \times 10^{-3} \text{ M}$  urea were mixed in 80 mL DI water to form a pink color solution, that was then transferred to teflon-lined autoclave with a piece of nickel foam comb electrode and was kept at  $120^\circ\text{C}$  for 6 h to grow  $\text{NiCo}_2(\text{CO}_3^{2-})_{1.5}(\text{OH})_3$  precursor on Ni foam. After cooling down to the room temperature, Ni foam was taken out and sonicated in DI water for 1 min in order to remove residual solid particles from the surface. Then,  $\text{NiCo}_2(\text{CO}_3^{2-})_{1.5}(\text{OH})_3$  precursor was chemically converted in-situ into  $\text{NiCo}_2\text{S}_4$  by a facile hydrothermal process.  $0.2 \text{ g}$   $\text{Na}_2\text{S} \cdot 9\text{H}_2\text{O}$  was dissolved in 40 mL water and transferred together with  $\text{NiCo}_2(\text{CO}_3^{2-})_{1.5}(\text{OH})_3$  precursor coated Ni foam to teflon-lined stainless steel autoclave, followed by heating to  $160^\circ\text{C}$  for 12 h. After heating, final product was washed with DI water and dried in vacuum at  $60^\circ\text{C}$ . Thus obtained  $\text{NiCo}_2\text{S}_4$  has a typical mass loading of  $2.5 \text{ mg cm}^{-2}$  on  $1200 \mu\text{m}$  Ni foam, which can be controlled based on the precursor concentration.

**Growth of CNF on Ni Foam:** First, freshly patterned Ni foam was cleaned by sonication in acetone, isopropanol, and deionized water. Then, Ni foam was taken out and annealed in air at  $500^\circ\text{C}$  for 2 h, the annealing process can roughen the Ni surface and thus prevents planar carbon layer formation. After annealing, it was cooled down and transferred to quartz tube and kept in  $700^\circ\text{C}$  for 15 min under Ar/ $\text{H}_2$  flow (Ar 50 sccm,  $\text{H}_2$  40 sccm) to reform metallic nickel from nickel oxide. Ar flow was stopped followed by introducing ethylene gas (20 sccm) into the quartz tube to grow CNF at same temperature for 2 h. Upon completion of growth process, the furnace was cooled down to room temperature under Ar flow. Before testing electrochemical performance of CNF/NF in the aqueous electrolyte, it was treated with nonthermal  $\text{O}_2$  plasma under 700 mTorr pressure (power 45 W) for 3 min to ensure proper wettability with aqueous electrolytes.

**Fabrication of the Hybrid Device:** Briefly, a mixture of PDMS elastomer and curing agent (mass ratio 10:1) was thoroughly mixed followed by degassing air bubbles under vacuum for 1 h at room temperature. Glass slides of  $1.5 \text{ cm} \times 2 \text{ cm}$  size (Fisher) were cleaned with a soap solution to remove the dirt followed by sonication in acetone, isopropanol, and DI water sequentially for 5 min each and then dried by blowing nitrogen ( $\text{N}_2$ ) gas. A simple rod coating technique was used in order to spread a thin film of PDMS on the glass before placement of  $\text{NiCo}_2\text{S}_4$ /NF and CNF/NF comb electrodes to define the coplanar hybrid microsupercapacitor structure. Since  $\text{NiCo}_2\text{S}_4$  is Faradaic type (positive electrode), while CNF being double layer type (negative), we refer to this device as  $\text{NiCo}_2\text{S}_4$ //CNF hybrid supercapacitor. Coplanar hybrid supercapacitors get nicely bonded to the glass by curing PDMS layer at  $80^\circ\text{C}$  for 30 min. The electrochemical measurements for the device were carried out by dipping the device in the electrolyte while predesigned pads were used for connection.

**Preparation of Polyvinylalcohol (PVA)/KOH Electrolyte:** Approximately 4 g of PVA was weighed and transferred into a 100 mL beaker containing 30 mL of deionized water. The mixture was heated at  $85^\circ\text{C}$  with constant stirring until a transparent solution of PVA was obtained. This was subsequently cooled to room temperature. Approximately, 2.24 g KOH was dissolved in 10 mL  $\text{H}_2\text{O}$  and was then added to the PVA solution and stirred gently for 24 h to obtain homogeneous PVA/KOH solution.



**Solid-State Device Assembly:** Shortly, gel electrolyte was carefully drop casted onto the coplanar device, then the device was left for slow drying at room temperature (25 °C) to form solid films. Since our device is thick, the drop casting process was repeated several times to ensure full coverage of the electrolyte.

**Material Characterization:** XRD patterns were collected by a Bruker diffractometer (D8 Advance) with Cu K $\alpha$  radiation,  $\lambda = 1.5406$  Å. The morphology and microstructure of the samples were characterized by SEM (Nova Nano 630, FEI), HRTEM (Titan 80–300 kV), and EDX column is equipped with the SEM. For TEM images, NiCo<sub>2</sub>S<sub>4</sub> and CNF powders were mechanically scratched off from Ni foam for characterization. XPS analysis was carried out using Kratos Axis Ultra DLD spectrometer equipped with a monochromatic Al K $\alpha$  X-ray source ( $h\nu = 1486.6$  eV) operating at 150 W, a multichannel plate and delay line detector under a vacuum of  $\approx 10^{-9}$  mbar. The high-resolution spectra were collected at fixed analyzer pass energy of 20 eV. Raman spectroscopy measurements were carried out on the powder samples using a micro-Raman spectrometer (LabRAM ARAMIS, Horiba-Jobin Yvon) with notch filters cutting at 100 cm<sup>-1</sup> using a Cobalt laser (473 nm, 5 mW at source) under Ar atmosphere.

**Electrochemical Characterization:** The electrochemical tests (cyclic voltammetry, galvanostatic charge-discharge, electrochemical cycling stability) were conducted at room temperature using a VMP3 electrochemical workstation (Bio-Logic, France). KOH of 1 M was used as the electrolyte for all electrochemical tests. The electrochemical impedance spectroscopy was measured using a Modulab (Solartron Analytical) electrochemical workstation in the frequency range from 100 kHz to 0.01 Hz at open circuit potential by applying a small sinusoidal potential of 10 mV signal. For three-electrode measurement, NiCo<sub>2</sub>S<sub>4</sub>/NF or CNF/NF were employed as working electrode with platinum and Ag/AgCl as counter and reference electrodes, respectively. Positive electrode was tested in the potential window of 0–0.5 V while negative electrode was tested in the negative window of 0 to –1 V. Finally, hybrid capacitor design comprising NiCo<sub>2</sub>S<sub>4</sub>/NF//CNF/NF was tested in both 1 M KOH and PVA/KOH gel electrolyte in two-electrode configuration.

## Supporting Information

Supporting Information is available from the Wiley Online Library or from the author.

## Acknowledgements

Research reported in this publication was supported by King Abdullah University of Science and Technology (KAUST). The authors thank Dr. Hanfeng Liang for several useful discussions, and the Advanced Nanofabrication, Imaging and Characterization Laboratory at KAUST for their excellent support.

Received: June 12, 2016

Revised: July 19, 2016

Published online: September 8, 2016

- [1] M. Beidaghi, Y. Gogotsi, *Energy Environ. Sci.* **2014**, *7*, 867.  
[2] a) P. Huang, D. Pech, R. Lin, J. K. McDonough, M. Brunet, P.-L. Taberna, Y. Gogotsi, P. Simon, *Electrochem. Commun.* **2013**, *36*, 53; b) D. Qi, Z. Liu, Y. Liu, W. R. Leow, B. Zhu, H. Yang, J. Yu, W. Wang, H. Wang, S. Yin, X. Chen, *Adv. Mater.* **2015**, *27*, 5559; c) J. Xu, G. Shen, *Nano Energy* **2015**, *13*, 131; d) B. Hsia, M. S. Kim, M. Vincent, C. Carraro, R. Maboudian, *Carbon* **2013**, *57*, 395.

- [3] D. Pech, M. Brunet, H. Durou, P. Huang, V. Mochalin, Y. Gogotsi, P. L. Taberna, P. Simon, *Nat. Nanotechnol.* **2010**, *5*, 651.  
[4] a) W. Liu, C. Lu, X. Wang, R. Y. Tay, B. K. Tay, *ACS Nano* **2015**, *9*, 1528; b) N. Kurra, N. A. Alhebshi, H. N. Alshareef, *Adv. Energy Mater.* **2015**, *5*, 1401303.  
[5] N. Kurra, C. Xia, M. N. Hedhili, H. N. Alshareef, *Chem. Commun.* **2015**, *51*, 10494.  
[6] a) N. Kurra, Q. Jiang, A. Syed, C. Xia, H. N. Alshareef, *ACS Appl. Mater. Interfaces* **2016**, *8*, 12748; b) Q. Jiang, N. Kurra, H. N. Alshareef, *Adv. Funct. Mater.* **2015**, *25*, 4976; c) N. Kurra, Q. Jiang, H. N. Alshareef, *Nano Energy* **2015**, *16*, 1.  
[7] a) S. Li, X. Wang, H. Xing, C. Shen, *J. Micromech. Microeng.* **2013**, *23*, 114013; b) C. Shen, X. Wang, S. Li, J. G. Wang, W. Zhang, F. Kang, *J. Power Sources* **2013**, *234*, 302.  
[8] a) H. Huo, Y. Zhao, C. Xu, *J. Mater. Chem. A* **2014**, *2*, 15111; b) K. Qiu, Y. Lu, J. Cheng, H. Yan, X. Hou, D. Zhang, M. Lu, X. Liu, Y. Luo, *Electrochim. Acta* **2015**, *157*, 62.  
[9] C. Yuan, J. Li, L. Hou, X. Zhang, L. Shen, X. W. D. Lou, *Adv. Funct. Mater.* **2012**, *22*, 4592.  
[10] D. Ping, C. Wang, X. Dong, Y. Dong, *Appl. Surf. Sci.* **2016**, *369*, 299.  
[11] Z. Chen, W. Ren, L. Gao, B. Liu, S. Pei, H. M. Cheng, *Nat. Mater.* **2011**, *10*, 424.  
[12] a) J. L. Yin, J. Y. Park, *Microporous Mesoporous Mater.* **2014**, *200*, 61; b) J. Zhang, F. Liu, J. P. Cheng, X. B. Zhang, *ACS Appl. Mater. Interfaces* **2015**, *7*, 17630; c) C. Wu, J. Cai, Q. Zhang, X. Zhou, Y. Zhu, P. K. Shen, K. Zhang, *ACS Appl. Mater. Interfaces* **2015**, *7*, 26512; d) C. Yuan, J. Li, L. Hou, X. Zhang, L. Shen, X. W. D. Lou, *Adv. Funct. Mater.* **2012**, *22*, 4592.  
[13] D. Cai, D. Wang, C. Wang, B. Liu, L. Wang, Y. Liu, Q. Li, T. Wang, *Electrochim. Acta* **2015**, *151*, 35.  
[14] a) P. Xu, J. Liu, P. Yan, C. Miao, K. Ye, K. Cheng, J. Yin, D. Cao, K. Li, G. Wang, *J. Mater. Chem. A* **2016**, *4*, 4920; b) X. F. Gong, J. P. Cheng, K. Y. Ma, F. Liu, L. Zhang, X. Zhang, *Mater. Chem. Phys.* **2016**, *173*, 317.  
[15] K.-J. Huang, J.-Z. Zhang, J.-L. Cai, *Electrochim. Acta* **2015**, *180*, 770.  
[16] D. Mohapatra, S. Badranyana, S. Parida, *RSC Adv.* **2016**, *6*, 14720.  
[17] C. Xia, P. Li, A. N. Gandi, U. Schwingenschlögl, H. N. Alshareef, *Chem. Mater.* **2015**, *27*, 6482.  
[18] L. Ma, Y. Hu, R. Chen, G. Zhu, T. Chen, H. Lv, Y. Wang, J. Liang, H. Liu, C. Yan, H. Zhu, Z. Tie, Z. Jin, J. Liu, *Nano Energy* **2016**, *24*, 139.  
[19] B. Yang, L. Yu, H. Yan, Y. Sun, Q. Liu, J. Liu, D. Song, S. Hu, Y. Yuan, L. Liu, J. Wang, *J. Mater. Chem. A* **2015**, *3*, 13308.  
[20] Z. Zhang, X. Wang, G. Cui, A. Zhang, X. Zhou, H. Xu, L. Gu, *Nanoscale* **2014**, *6*, 3540.  
[21] A. Ferris, S. Garbarino, D. Guay, D. Pech, *Adv. Mater.* **2015**, *27*, 6625.  
[22] C. Wan, L. Yuan, H. Shen, *Int. J. Electrochem. Sci.* **2014**, *9*, 4024.  
[23] J. Wang, J. Polleux, J. Lim, B. Dunn, *J. Phys. Chem. C* **2007**, *111*, 14925.  
[24] V. Augustyn, P. Simon, B. Dunn, *Energy Environ. Sci.* **2014**, *7*, 1597.  
[25] J. R. McDonough, J. W. Choi, Y. Yang, F. La Mantia, Y. Zhang, Y. Cui, *Appl. Phys. Lett.* **2009**, *95*, 243109.  
[26] N. Kurra, V. S. Bhadrani, C. Narayana, G. U. Kulkarni, *ACS Appl. Mater. Interfaces* **2012**, *4*, 1030.  
[27] A. Laheäär, P. Przygocki, Q. Abbas, F. Béguin, *Electrochem. Commun.* **2015**, *60*, 21.  
[28] a) P. Huang, C. Lethien, S. Pinaud, K. Brousse, R. Laloo, V. Turq, M. Respaud, A. Demortière, B. Daffos, P. Taberna, *Science* **2016**, *351*, 691; b) J. Lin, Z. Peng, Y. Liu, F. Ruiz-Zepeda, R. Ye, E. L. Samuel, M. J. Yacamán, B. I. Yakobson, J. M. Tour, *Nat. Commun.* **2014**, *5*, 5714.  
[29] J. S. Kim, D. Ko, D. J. Yoo, D. S. Jung, C. T. Yavuz, N. I. Kim, I. S. Choi, J. Y. Song, J. W. Choi, *Nano Lett.* **2015**, *15*, 2350.